J. Fluid Mech., page 1 of 27. © Cambridge University Press 2012
doi:10.1017/jfm.2012.151

First instability of the flow of shear-thinning and shear-thickening fluids past a circular cylinder

Iman Lashgari[1], Jan O. Pralits[2,3], Flavio Giannetti[2] and Luca Brandt[1]†

[1] Linné Flow Centre, KTH Mechanics, S-100 44 Stockholm, Sweden
[2] DIIN, University of Salerno, via Ponte don Melillo, 84084 Fisciano (SA), Italy
[3] DICAT, University of Genova, via Montallegro 1, 16145 Genova, Italy

(Received 31 October 2011; revised 9 February 2012; accepted 19 March 2012)

The first bifurcation and the instability mechanisms of shear-thinning and shear-thickening fluids flowing past a circular cylinder are studied using linear theory and numerical simulations. Structural sensitivity analysis based on the idea of a 'wavemaker' is performed to identify the core of the instability. The shear-dependent viscosity is modelled by the Carreau model where the rheological parameters, i.e. the power-index and the material time constant, are chosen in the range $0.4 \leqslant n \leqslant 1.75$ and $0.1 \leqslant \lambda \leqslant 100$. We show how shear-thinning/shear-thickening effects destabilize/stabilize the flow dramatically when scaling the problem with the reference zero-shear-rate viscosity. These variations are explained by modifications of the steady base flow due to the shear-dependent viscosity; the instability mechanisms are only slightly changed. The characteristics of the base flow, drag coefficient and size of recirculation bubble are presented to assess shear-thinning effects. We demonstrate that at critical conditions the local Reynolds number in the core of the instability is around 50 as for Newtonian fluids. The perturbation kinetic energy budget is also considered to examine the physical mechanism of the instability.

Key words: instability, non-Newtonian flows, wakes

1. Introduction

The aim of the present work is to study the effects of shear-dependent viscosity on the appearance of the first instability for the flow past a circular cylinder. We consider shear-thinning and shear-thickening fluids obeying the Carreau–Yasuda rheological law. The flow past a circular cylinder is chosen as the classical example of bluff-body flows. Although an idealized configuration, flows past circular cylinders are relevant to many industrial applications. Some examples are tubular and pin-type heat exchangers, filtration screens and membrane-based separation modules (see e.g. Panda & Chhabra 2010).

From a stability point of view, the cylinder flow displays intrinsic dynamics and the spatial distribution of the disturbance synchronizes in space. The instability of the cylinder flow has been extensively studied in the past for Newtonian fluids. Based on these previous works, Mossaz, Jay & Magnin (2010), among many, describe the

† Email address for correspondence: luca@mech.kth.se

different regimes observed when varying the Reynolds number. The flow changes from creeping flow with no separation to laminar flow with two symmetrical steady vortices at Reynolds number ∼6. The length of the steady recirculation regions increases linearly with the Reynolds number (e.g. Giannetti & Luchini 2007). The transition to unsteady periodic flow (i.e. the Hopf bifurcation) of the two-dimensional flow is at Reynolds number ∼47 (Provansal, Mathis & Boyer 1987). Finally a three-dimensional wake appears when the Reynolds number is ∼190 (Barkley & Henderson 1996). In this work, we focus on the first bifurcation to unsteady flow and use a sensitivity analysis to understand the instability mechanisms.

1.1. *Cylinder flow of non-Newtonian fluids*

Recently several investigations have been conducted to understand the non-Newtonian effects on the characteristics of the flow around a circular cylinder in different regimes.

As regards shear-thinning fluid flowing past a cylinder, Coelho & Pinho (2003*a*,*b*) and Coelho & Pinho (2004) carried out experimental studies on the vortex-shedding flow regimes of both Newtonian fluids and shear-thinning weakly elastic polymer solutions. The Reynolds number was varied from 50 to 9000 including laminar vortex shedding, transition and shear-layer transition regimes. It was shown that shear-thinning gives rise to a reduction of the cylinder boundary-layer thickness and a decrease of the diffusion length which increases the Strouhal number. Conversely, fluid elasticity is responsible for an elongation of the formation region which results in a decrease of the Strouhal number.

Only a few studies have considered shear-dependent viscosity. Sivakumar, Bharti & Chhabra (2006) and Patnana, Bharti & Chhabra (2009) investigated lift and drag coefficients as well as instantaneous streamlines and vortices for the flow past a stationary and a rotating cylinder by means of numerical simulations. These authors examined both shear-thinning and shear-thickening fluids, using the power law, in the range of creeping flow up to Reynolds number equal to 140. In the case of a stationary cylinder, the drag coefficient decreases with shear-thinning at a fixed value of Reynolds number. For rotating cylinders, the viscosity variation influences the drag and the lift coefficients of low-Reynolds-number flows more than those of high-Reynolds-number flows. Nejat, Abdollahi & Vahidkhah (2011) simulate the power-law flow past a series of tandem arrangement of two cylinders in a confined domain, using a lattice Boltzmann algorithm. For a Reynolds number equal to 40, the drag on the upstream cylinder is one order of magnitude larger than on the one downstream for cylinder spacing up to two times the cylinder diameter. Mossaz *et al.* (2010) simulate a Herschel–Bulkley viscoplastic fluid behind a circular cylinder in order to obtain a criterion for the appearance of non-stationary regimes at subcritical Reynolds numbers. The frequency of vortex shedding in the supercritical regime decreases with the Oldroyd number and it is therefore concluded that viscoplastic effects stabilize the flow.

As seen from the above discussion, several efforts have considered the flow of a viscoelastic fluid past a cylinder, see among others Sarpkaya, Rainey & Kell (1973) and Pipe & Monkewitz (2006). In a recent study, Richter, Iaccarino & Shaqfeh (2010) investigate a dilute solution of polymers at Reynolds numbers of 100 and 300 via numerical simulations of the FENE-P model. In particular at Reynolds number equal to 100, an increase in polymer extensibility elongates the recirculating region behind the cylinder and increases the average drag. At larger Reynolds number, polymer elasticity suppresses the secondary three-dimensional mode which dominates the structure of the near-wake for Newtonian fluids. Later, the same authors investigated

the viscoelastic effects on the stability of the cylinder wake using linear theory (Richter, Shaqfeh & Iaccarino 2011). They found that viscoelasticity modifies the underlying base flow which results in a reduction of vorticity intensity and strain rate in the wake and successively a decrease in the production of perturbation energy.

1.2. *Instability in shear-thinning fluids*

The pseudo-plastic fluids (shear-thinning fluids) can be classified as inelastic non-Newtonian fluids in which the viscosity is decreasing with the shear rate. The two most popular rheological laws for shear-dependent viscosity are the power-law model and the Carreau–Yasuda model. Nouar & Frigaard (2009) note that the power-law model can only be used for a limited range of shear rates, while the Carreau–Yasuda model is more realistic and has the flexibility to fit a wide range of experimental data. Coelho & Pinho (2004) experimentally showed that the Carreau model can be fitted to a solution of dilute polymers with different degrees of shear-thinning for the flow past a cylinder. Nouar, Bottaro & Brancher (2007) choose the Carreau model because of its capability to model steady shear, complex viscosity, stress growth and the stress relaxation function. In this work the Carreau law is chosen to model viscosity of shear-thinning and shear-thickening fluid past a circular cylinder.

The stability of a variety of shear-thinning fluids has already been studied for canonical parallel flows, e.g. circular Couette flow, channel flow, mixed plane Couette and Poiseuille flow and gravity-driven flow over an inclined plane. Caton (2006) presented linear stability results of a power-law fluid for circular Couette flow. For small gaps between the two cylinders, the critical Reynolds number for the onset of instability reduces with increasing shear-thinning. Nouar *et al.* (2007) used the Carreau rheological law model to investigate modal and non-modal instability of channel flow. Nouar & Frigaard (2009) analysed the instability of the mixed plane Couette and Poiseuille flow for a shear-thinning fluid, also using the Carreau law. These authors showed that the production of kinetic energy in the critical layer next to the fixed wall controls the stability of the flow. Milleta, Rousset & Hadid (2009) showed the stabilizing effects of shear-thinning on the flow of two layers of fluid with different density over an inclined plane using linear theory.

Here we study how shear-thinning and shear-thickening effects vary the critical Reynolds number for the cylinder flow. We present the first global stability analysis for this two-dimensional configuration and shear-dependent inelastic fluids. Note that recently Panda & Chhabra (2010) investigated by numerical simulations the critical Reynolds number of the power-law cylinder flow for the range of $0.3 < n < 1.8$. They reported that the critical Reynolds number first increases with the power index, to about $n \approx 0.6$, and then decreases sharply. (In contrast, we show in this work, using the Carreau law, that the critical Reynolds number is always decreasing on increasing the shear-thinning.)

1.3. *Structural sensitivity*

Structural sensitivity analysis is used to determine the instability mechanism that initiates the transition to an unsteady flow (Chomaz 2005). Giannetti & Luchini (2007) analysed the instability mechanism of the flow past a stationary cylinder and introduced the concept of structural sensitivity. The spatial structure of the modes shows maximum amplitude of the perturbation downstream of the cylinder. However, highest receptivity is found in the near wake (close to the cylinder). Structural sensitivity identifies the core of instability: this is associated with the location in space where a feedback provides the largest shift of the eigenvalues. The disturbance

equation is forced by a local force–velocity feedback modelling the effect of a small control device. Such a device has two distinct effects: in the quasi-static limit, it forces the disturbance through a feedback like that studied by Giannetti & Luchini (2007). Nevertheless, it would also modify the base flow. Marquet, Sipp & Jacquin (2008) studied the sensitivity to base-flow modifications of the flow past a circular cylinder, still related to the maximum variation of the eigenvalue. The authors identified the region that most contributes to the onset of vortex shedding. The sensitivity to steady forcing determines the regions which can stabilize the unstable global modes. This approach is used in Marquet *et al.* (2009) to control separation in an S-shaped duct. Pralits, Brandt & Giannetti (2010) used the same formulation as Giannetti & Luchini (2007) to examine the first and second shedding modes of flow past a rotating cylinder. These authors compared their results with the analysis of the perturbation kinetic energy budget. They also suggested placing a small cylinder close to the main rotating cylinder to control the instabilities based on the sensitivity maps originating from the structural sensitivity analysis. Other investigations worth mentioning regarding the effect of base-flow modifications are Bottaro, Corbett & Luchini (2003) for plane Couette flow, Meliga, Sipp & Chomaz (2010*a*,*b*) who analyse compressible axisymmetric wake flows and Alizard, Robinet & Rist (2010) concerning the flow formed by the intersection of two perpendicular flat plates.

A recent review of linear approaches to sensitivity and control can be found in Sipp *et al.* (2010). The authors describe the dynamics of instabilities and introduce open-loop and closed-loop control strategies to suppress them. Sensitivity of globally stable flows to transient disturbance growth is considered in Brandt *et al.* (2011).

The paper is organized as follows. The viscosity model and stability equations are given in § 2. After introducing the numerical method in § 3, we present results for shear-thinning and shear-thickening fluids in §§ 4 and 5. Section 6 reports a summary of the main conclusions and a final discussion.

2. Problem formulation

2.1. *Viscosity model*

The Carreau–Yasuda model describes the behaviour of fluids with shear-dependent viscosity, so called shear-thinning and shear-thickening fluids. The relation between viscosity and deformation rate is given by

$$\mu = \frac{\hat{\mu}_\infty}{\hat{\mu}_0} + \left[1 - \frac{\hat{\mu}_\infty}{\hat{\mu}_0}\right][1 + (\lambda\dot{\gamma})^a]^{(n-1)/a}. \tag{2.1}$$

In this expression, $\hat{\mu}_0$ and $\hat{\mu}_\infty$ are the zero-shear-rate and infinite-shear-rate viscosities, set to 1 and 0.001 in this work. μ is non-dimensional and normalized with respect to $\hat{\mu}_0$. The second invariant of the strain-rate tensor is denoted as $\dot{\gamma}$ and is determined by the dyadic product $\dot{\gamma} = ((1/2)\boldsymbol{G} : \boldsymbol{G})^{1/2}$, where $\boldsymbol{G} = \nabla\boldsymbol{u} + (\nabla\boldsymbol{u})^{\mathrm{T}}$ (see Bird *et al.* 1987). The non-dimensional parameter a describes the transition between the zero-shear-rate viscosity and the infinite-shear-rate viscosity (Bird *et al.* 1987). The Carreau–Yasuda model can be fitted to the rheological behaviour of many polymeric solutions when $a = 2$, also denoted the Carreau model. The power-law index n characterizes the fluid behaviour: (i) shear-thinning when $n < 1$; (ii) Newtonian when $n = 1$; and (iii) shear-thickening when $n > 1$. Here, λ is the material time constant. Newtonian fluid is

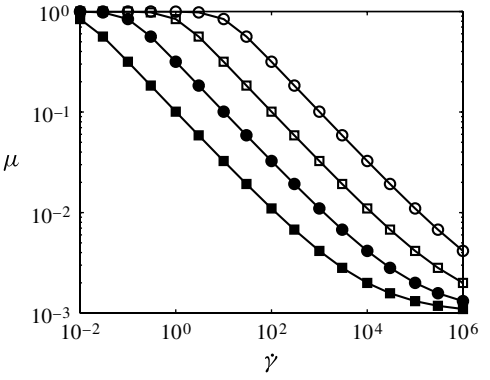

FIGURE 1. Viscosity μ of Carreau-law model versus shear rate $\dot{\gamma}$ for $n = 0.5$: ◯, $\lambda = 0.1$; □, $\lambda = 1$; ●, $\lambda = 10$; ■, $\lambda = 100$.

also obtained setting $\lambda = 0$, and for large values of λ the Carreau model is reduced to the power-law model

$$\mu = K\,(\dot{\gamma})^{n-1}, \tag{2.2}$$

where K is a consistency factor. A logarithmic plot of the viscosity versus the shear rate for the Carreau-law model provides intuition on how the viscosity of a shear-thinning fluid decreases when increasing the shear rate. In figure 1 the viscosity is shown as a function of $\dot{\gamma}$ for different λ and a fixed value $n = 0.5$ of the power index. The shear-thinning effects become more evident on increasing λ and the viscosity tends to the asymptotic value μ_∞ for large shear rates.

2.2. *Governing equation: base-flow and stability problem*

The continuity and Navier–Stokes equations with shear-dependent viscosity govern the flow past a stationary circular cylinder of an incompressible shear-thinning fluid. The non-dimensional form of the governing equations is

$$\frac{\partial \tilde{\boldsymbol{u}}}{\partial t} + \tilde{\boldsymbol{u}} \cdot \boldsymbol{\nabla}\tilde{\boldsymbol{u}} = -\boldsymbol{\nabla} p + \frac{1}{Re}\boldsymbol{\nabla} \cdot [\mu(\tilde{\boldsymbol{u}})(\boldsymbol{\nabla}\tilde{\boldsymbol{u}} + \boldsymbol{\nabla}\tilde{\boldsymbol{u}}^{\mathrm{T}})], \tag{2.3}$$

$$\boldsymbol{\nabla} \cdot \tilde{\boldsymbol{u}} = 0, \tag{2.4}$$

where $\tilde{\boldsymbol{u}} = (\tilde{u}, \tilde{v}, \tilde{w})$ is a vector containing the non-dimensional velocity components, p is the non-dimensional pressure and μ the viscosity defined by the Carreau model introduced above. The Reynolds number is here defined by

$$Re = \frac{\rho U_\infty D}{\hat{\mu}_0}, \tag{2.5}$$

where $\hat{\mu}_0$ is the viscosity at zero shear rate, U_∞ is the free-stream velocity, D the cylinder diameter and ρ the fluid density.

To perform a linear stability analysis, we introduce small perturbations in the flow and study their spatial and temporal evolution. The flow variables are decomposed into a two-dimensional steady base flow and a small unsteady perturbation, in general three-dimensional. For shear-thinning and -thickening fluids the decomposition includes not

only the velocity and the pressure but also the viscosity μ:

$$\tilde{\boldsymbol{u}}(x,y,z,t) = \boldsymbol{U}_b(x,y) + \boldsymbol{u}'(x,y,z,t), \tag{2.6a}$$

$$p(x,y,z,t) = P_b(x,y) + p'(x,y,z,t), \tag{2.6b}$$

$$\mu(x,y,z,t) = \mu_b(x,y) + \mu'(x,y,z,t). \tag{2.6c}$$

The base-flow variables $\boldsymbol{U}_b$, P_b and μ_b are time independent and satisfy the steady Navier–Stokes equation

$$\boldsymbol{U}_b \cdot \boldsymbol{\nabla}\boldsymbol{U}_b = -\boldsymbol{\nabla}P_b + \frac{1}{Re}\boldsymbol{\nabla}\cdot[\mu_b(\boldsymbol{U}_b)(\boldsymbol{\nabla}\boldsymbol{U}_b + \boldsymbol{\nabla}\boldsymbol{U}_b^{\mathrm{T}})], \tag{2.7}$$

$$\boldsymbol{\nabla}\cdot\boldsymbol{U}_b = 0. \tag{2.8}$$

To derive the linearized stability equations, we first define the viscosity fluctuations by the linear term of the Taylor expansion of the viscosity function $\mu(\dot{\gamma})$:

$$\mu' = \dot{\gamma}_{ij}(\boldsymbol{u}')\frac{\partial\mu}{\partial\dot{\gamma}_{ij}}(\boldsymbol{U}_b), \tag{2.9}$$

where μ' is a scalar quantity that can be expressed as the inner product of a vector $\boldsymbol{B}$ and the velocity perturbation. For the sake of clarity, we present here the derivation only for two-dimensional perturbations which are found to be the first to become unstable; in this case the viscosity fluctuation can be written

$$\mu' = \boldsymbol{B}\,(\boldsymbol{U}_b)^{\mathrm{T}}\cdot\boldsymbol{u}' = [X1\,X2]\cdot\begin{bmatrix}u'\\v'\end{bmatrix}, \tag{2.10}$$

with $X1$ and $X2$ defined as

$$X1 = 2\frac{\partial\mu}{\partial\dot{\gamma}_{11}}(\boldsymbol{U}_b)\frac{\partial}{\partial x} + 2\frac{\partial\mu}{\partial\dot{\gamma}_{12}}(\boldsymbol{U}_b)\frac{\partial}{\partial y}, \tag{2.11a}$$

$$X2 = 2\frac{\partial\mu}{\partial\dot{\gamma}_{12}}(\boldsymbol{U}_b)\frac{\partial}{\partial x} + 2\frac{\partial\mu}{\partial\dot{\gamma}_{22}}(\boldsymbol{U}_b)\frac{\partial}{\partial y}. \tag{2.11b}$$

Introducing the decomposition (2.6*a*), (2.6*b*) and (2.6*c*) into (2.3) and (2.4) and neglecting higher-order terms, we can write the linearized stability equations

$$\frac{\partial\boldsymbol{u}'}{\partial t} + \boldsymbol{L}(\boldsymbol{U}_b, Re)\boldsymbol{u}' + \boldsymbol{\nabla}p' = 0, \tag{2.12}$$

$$\boldsymbol{\nabla}\cdot\boldsymbol{u}' = 0, \tag{2.13}$$

where the operator $\boldsymbol{L}$ is

$$\boldsymbol{L}(\boldsymbol{U}_b, Re)\boldsymbol{u}' = \boldsymbol{u}'\cdot\boldsymbol{\nabla}\boldsymbol{U}_b + \boldsymbol{U}_b\cdot\boldsymbol{\nabla}\boldsymbol{u}' - \frac{1}{Re}\boldsymbol{\nabla}\cdot[\mu(\boldsymbol{U}_b)(\boldsymbol{\nabla}\boldsymbol{u}' + (\boldsymbol{\nabla}\boldsymbol{u}')^{\mathrm{T}}) + (\boldsymbol{B}(\boldsymbol{U}_b)\cdot\boldsymbol{u}')(\boldsymbol{\nabla}\boldsymbol{U}_b + \boldsymbol{\nabla}\boldsymbol{U}_b^{\mathrm{T}})]. \tag{2.14}$$

Perturbations are assumed to decay far from the cylinder and vanish at the cylinder surface. Solutions of the stability problem are sought in the form

$$\boldsymbol{u}'(x,y,z,t) = \hat{\boldsymbol{u}}(x,y)\exp(\sigma t + \mathrm{i}\beta z), \quad p'(x,y,z,t) = \hat{p}(x,y)\exp(\sigma t + \mathrm{i}\beta z), \tag{2.15}$$

where β is the spanwise wavenumber introduced to exploit the homogeneity in the spanwise direction z.

Finally the stability problem reduces to the following eigenvalue problem:

$$\sigma\hat{\boldsymbol{u}} + \boldsymbol{L}(\boldsymbol{U}_b, Re)\hat{\boldsymbol{u}} + \nabla\hat{p} = 0, \tag{2.16}$$

$$\nabla \cdot \hat{\boldsymbol{u}} = 0. \tag{2.17}$$

The complex number σ is the eigenvalue of our stability problem and the complex field $\hat{\boldsymbol{q}} = (\hat{\boldsymbol{u}}, \hat{p})$ the corresponding eigenmode. The real and imaginary parts of σ represent the growth rate and circular frequency of the perturbation.

2.3. *Structural sensitivity and energy budget*

Structural sensitivity analysis based on the idea of a 'wavemaker' was introduced in Giannetti & Luchini (2007) to identify the location of the core of a global instability. The wavemaker is the region in the flow where variations in the structure of the problem provide the largest drift of the eigenvalues. This will be considered in parallel with production of perturbation kinetic energy. In this section, we follow the derivation of the structural sensitivity as presented in Pralits *et al.* (2010) and include viscosity perturbation in the formulation. We start with the perturbed eigenvalue problem

$$\sigma'\hat{\boldsymbol{u}}' + \boldsymbol{L}(\boldsymbol{U}_b, Re)\hat{\boldsymbol{u}}' + \nabla\hat{p}' = \delta H(\hat{\boldsymbol{u}}', \hat{p}'), \tag{2.18}$$

$$\nabla \cdot \hat{\boldsymbol{u}}' = 0, \tag{2.19}$$

where δH is the generalized structural perturbation. It is assumed to be a momentum force localized in space and proportional to the local velocity perturbation defined by a (2×2) coupling matrix $\delta\boldsymbol{M}_0$ and the delta function

$$\delta H(\hat{\boldsymbol{u}}', \hat{p}') = \delta\boldsymbol{M}(x, y) \cdot \hat{\boldsymbol{u}}' = \delta(x - x_0, y - y_0)\delta\boldsymbol{M}_0 \cdot \hat{\boldsymbol{u}}'. \tag{2.20}$$

Neglecting the higher-order terms, variations of the eigenvalue $\delta\sigma$ and of the corresponding eigenfunction $(\delta\hat{\boldsymbol{u}}, \delta\hat{p})$ satisfy the following expression:

$$\sigma\delta\hat{\boldsymbol{u}} + \boldsymbol{L}(\boldsymbol{U}_b, Re)\delta\hat{\boldsymbol{u}} + \nabla\delta\hat{p} = -\delta\sigma\hat{\boldsymbol{u}} + \delta M \cdot \hat{\boldsymbol{u}}, \tag{2.21}$$

$$\nabla \cdot \delta\hat{\boldsymbol{u}} = 0. \tag{2.22}$$

We introduce the Lagrange identity as a function of the differentiable direct field $\boldsymbol{q} = (\boldsymbol{u}, p)$ and its adjoint field $\boldsymbol{g}^+ = (\boldsymbol{f}^+, m^+)$:

$$\begin{aligned}&[(\sigma\hat{\boldsymbol{u}} + \boldsymbol{L}(\boldsymbol{U}_b, Re)\hat{\boldsymbol{u}} + \nabla\hat{p}) \cdot \hat{\boldsymbol{f}^+} + (\nabla \cdot \hat{\boldsymbol{u}}) \cdot m^+] \\ &\quad + [\hat{\boldsymbol{u}} \cdot (-\sigma\hat{\boldsymbol{f}^+} + \boldsymbol{L}^+(\boldsymbol{U}_b, Re) + \nabla m^+) + \hat{p}\nabla \cdot \hat{\boldsymbol{f}}^+] = \nabla \cdot \boldsymbol{J}(\hat{\boldsymbol{q}}, \hat{\boldsymbol{g}}^+),\end{aligned} \tag{2.23}$$

where $\boldsymbol{J}$ is the bilinear concomitant

$$\begin{aligned}\boldsymbol{J}(\hat{\boldsymbol{q}}, \hat{\boldsymbol{g}}^+) = \boldsymbol{U}_b(\hat{\boldsymbol{u}} \cdot \hat{\boldsymbol{f}}^+) + \frac{1}{Re}\Big[&\mu(\boldsymbol{U}_b)(\nabla\hat{\boldsymbol{f}}^+ + (\nabla\hat{\boldsymbol{f}}^+)^{\mathrm{T}}) \cdot \hat{\boldsymbol{u}} - \mu(\boldsymbol{U}_b)(\nabla\hat{\boldsymbol{u}} + \nabla\hat{\boldsymbol{u}}^{\mathrm{T}}) \cdot \hat{\boldsymbol{f}}^+ \\ &- (\boldsymbol{B}(\boldsymbol{U}_b) \cdot \hat{\boldsymbol{u}})(\nabla\boldsymbol{U}_b + \nabla\boldsymbol{U}_b^{\mathrm{T}}) \cdot \hat{\boldsymbol{f}}^+\Big] + m^+\hat{\boldsymbol{u}} + \hat{p}\hat{\boldsymbol{f}}^+.\end{aligned} \tag{2.24}$$

Using (2.23), the equation for the adjoint field $\hat{\boldsymbol{g}}^+(x, y) = (\hat{\boldsymbol{f}}^+, \hat{m}^+)$ is

$$-\sigma\hat{\boldsymbol{f}^+} + \boldsymbol{L}^+(\boldsymbol{U}_b, Re) + \nabla m^+ = 0, \tag{2.25}$$

$$\nabla \cdot \hat{\boldsymbol{f}}^+ = 0, \tag{2.26}$$

where $\boldsymbol{L}^+$ is the adjoint operator of the linearized Navier–Stokes equation

$$\boldsymbol{L}^+(\boldsymbol{U}_b, Re)\hat{\boldsymbol{f}}^+ = \boldsymbol{U}_b \cdot \boldsymbol{\nabla}\hat{\boldsymbol{f}}^+ - \boldsymbol{\nabla}\boldsymbol{U}_b \cdot \hat{\boldsymbol{f}}^+ + \frac{1}{Re}\left[\mu(\boldsymbol{U}_b)(\Delta\hat{\boldsymbol{f}}^+ + (\Delta\hat{\boldsymbol{f}}^+)^{\mathrm{T}}) + (\boldsymbol{\nabla}\boldsymbol{U}_b + \boldsymbol{\nabla}\boldsymbol{U}_b^{\mathrm{T}}) \cdot \boldsymbol{\nabla}\hat{\boldsymbol{f}}^+ \boldsymbol{B}(\boldsymbol{U}_b)\right]. \tag{2.27}$$

Considering (2.21), (2.22), (2.23), (2.25) and (2.26), taking the integral over the whole domain D, we obtain the following:

$$-\delta\sigma \int_D \hat{\boldsymbol{f}}^+ \cdot \hat{\boldsymbol{u}}\, \mathrm{d}A + \int_D \hat{\boldsymbol{f}}^+ \cdot \delta\boldsymbol{M} \cdot \hat{\boldsymbol{u}}\, \mathrm{d}A = \int_{\partial D} \boldsymbol{J}(\hat{\boldsymbol{q}}, \hat{\boldsymbol{g}}^+) \cdot \boldsymbol{n}\, \mathrm{d}l. \tag{2.28}$$

Note that the boundary conditions are set in such a way that the right-hand side of (2.28) becomes zero. Introducing the sensitivity tensor

$$\boldsymbol{S}(x_0, y_0) = \frac{\boldsymbol{f}^+(x_0, y_0)\hat{\boldsymbol{u}}(x_0, y_0)}{\displaystyle\int_D \hat{\boldsymbol{f}}^+ \cdot \hat{\boldsymbol{u}}\, \mathrm{d}A}, \tag{2.29}$$

the expression for the eigenvalue drift is

$$\delta\sigma(x_0, y_0) = \frac{\displaystyle\int_D \hat{\boldsymbol{f}}^+ \cdot \delta\boldsymbol{M} \cdot \hat{\boldsymbol{u}}\, \mathrm{d}A}{\displaystyle\int_D \hat{\boldsymbol{f}}^+ \cdot \hat{\boldsymbol{u}}\, \mathrm{d}A} = \frac{\hat{\boldsymbol{f}}^+ \cdot \delta\boldsymbol{M}_0 \cdot \hat{\boldsymbol{u}}}{\displaystyle\int_D \hat{\boldsymbol{f}} \cdot \hat{\boldsymbol{u}}\, \mathrm{d}A} = \boldsymbol{S} : \delta\boldsymbol{M}_0 = S_{ij}\delta M_{0ij}. \tag{2.30}$$

The core of instability can be identified by different norms of the tensor $\boldsymbol{S}$. Here we will show the spectral norm, the largest singular value of the tensor $\boldsymbol{S}$.

2.3.1. *Structural sensitivity to base-flow modifications*

To clarify the role of the base flow in the instability and gain information about the effect of passive control devices, we investigate the structural sensitivity due to base-flow modifications. Here, we briefly outline the formulation presented in Pralits *et al.* (2010). The expression for the eigenvalue drift is derived in two steps: first we consider the sensitivity to an arbitrary variation of the base flow and, second, we assume that such a variation is induced by a steady structural forcing to the steady Navier–Stokes equations, where the structural perturbation is of the same form as that discussed above (proportional to the local velocity). An arbitrary variation of the base flow gives the following perturbed eigenvalue problem:

$$\sigma\delta\hat{\boldsymbol{u}} + \boldsymbol{L}(\boldsymbol{U}_b, Re)\delta\hat{\boldsymbol{u}} + \boldsymbol{\nabla}\delta\hat{p} = -[\delta\sigma\hat{\boldsymbol{u}} + \delta\boldsymbol{U}_b \cdot \boldsymbol{\nabla}\hat{\boldsymbol{u}} + \hat{\boldsymbol{u}} \cdot \boldsymbol{\nabla}\delta\boldsymbol{U}_b], \tag{2.31}$$

$$\boldsymbol{\nabla} \cdot \delta\hat{\boldsymbol{u}} = 0, \tag{2.32}$$

which can be subject to the same analysis as in the previous section to obtain an expression for the sensitivity. A base-flow variation due to a small structural perturbation can be written as a solution of the steady linearized equations

$$\boldsymbol{L}(\boldsymbol{U}_b, Re)\delta\boldsymbol{U}_b + \boldsymbol{\nabla}\delta P_b = \delta M \cdot \boldsymbol{U}_b, \tag{2.33}$$

$$\boldsymbol{\nabla} \cdot \delta\boldsymbol{U}_b = 0. \tag{2.34}$$

Following the derivation in Pralits *et al.* (2010), the Lagrange identity is built upon the base flow $\delta Q_b(x, y) = \{\delta\boldsymbol{U}_b, \delta P_b\}$ and on its adjoint field $G_b^+(x, y) = \{\boldsymbol{f}_b^+, m_b^+\}$,

so that the eigenvalue drift can be expressed as

$$\delta\sigma(x_0, y_0) = \frac{\int_D \boldsymbol{f}_b^+ \cdot \delta\boldsymbol{M} \cdot \hat{\boldsymbol{U}}_b \,\mathrm{d}A}{\int_D \hat{\boldsymbol{f}}^+ \cdot \hat{\boldsymbol{u}} \,\mathrm{d}A} = \frac{\boldsymbol{f}_b^+(x_0, y_0) \cdot \delta\boldsymbol{M}_0 \cdot \boldsymbol{U}_b(x_0, y_0)}{\int_D \hat{\boldsymbol{f}}^+ \cdot \hat{\boldsymbol{u}} \,\mathrm{d}A}$$
$$= \boldsymbol{S}_b(x_0, y_0) : \delta\boldsymbol{M}_0, \tag{2.35}$$

where

$$\boldsymbol{S}_b(x_0, y_0) = \frac{\boldsymbol{f}_b^+(x_0, y_0)\boldsymbol{U}_b(x_0, y_0)}{\int_D \hat{\boldsymbol{f}}^+ \cdot \hat{\boldsymbol{u}} \,\mathrm{d}A}. \tag{2.36}$$

Hence different norms of the tensor $\boldsymbol{S}_b$ represent the structural sensitivity to a small local force proportional to the local base-flow velocity.

2.3.2. *Perturbation kinetic energy budget*

Analysis of perturbation kinetic energy is a classical approach to examine instability mechanisms. The velocity fluctuations are complex functions (see (2.15)), and thus the evolution equation for perturbation kinetic energy is obtained by multiplying the linearized stability equations (2.12) and (2.13) by the complex conjugate of the velocity fluctuation $u_i'^*$ (in the following * denotes the complex conjugate). The kinetic energy budget reads

$$\frac{\mathrm{d}(E)}{\mathrm{d}t} = \frac{\partial}{\partial x_j}\left[-\frac{1}{2}U_j u_i' u_i'^* - \frac{1}{2}(u_j'^* p' + u_j' p'^*) + \frac{1}{Re}\mu_b(u_i'^* e_{ij} + u_i' e_{ij}^*)\right.$$
$$\left. + \frac{1}{Re}E_{ij}(u_i'^* \mu' + u_i' \mu'^*)\right] - \frac{1}{2}(u_i'^* u_j' + u_i' u_j'^*)\frac{\partial U_i}{\partial x_j} - \frac{2}{Re}\mu_b(e_{ij}e_{ij}^*)$$
$$- \frac{1}{Re}(\mu' e_{ij}^* E_{ij} + \mu'^* e_{ij} E_{ij}), \tag{2.37}$$

where E_{ij} and e_{ij} are the shear-rate tensors corresponding to the base flow and perturbations and $E = (1/2)(u_i' u_i'^*)$ is the pertubation kinetic energy. The first term on the right-hand side of the (2.37) is the divergence of four transport terms that do not contribute to the energy amplification once integrated across the domain (perturbations are assumed to decay to zero far away from the cylinder). The second and the third terms are the classic production and viscous dissipation. The last term is an additional term due to the non-Newtonian effects. Using the Carreau model (2.1) and the expression for the viscosity fluctuation (2.9), we obtain

$$\mu_b = \frac{\hat{\mu}_\infty}{\hat{\mu}_0} + \left[1 - \frac{\hat{\mu}_\infty}{\hat{\mu}_0}\right][1 + 2\lambda^2 E_{ij}^2]^{(n-1)/2}, \tag{2.38}$$

$$\mu' = e_{ij}\frac{\partial \mu_b}{\partial E_{ij}} = A e_{ij} E_{ij}, \tag{2.39}$$

where the coefficient

$$A = \lambda^2\left[1 - \frac{\hat{\mu}_\infty}{\hat{\mu}_0}\right]\left[\frac{n-1}{2}\right]\left[1 + \frac{\lambda^2}{2}E_{ij}^2\right]^{(n-3)/2}. \tag{2.40}$$

The last term on the right-hand side of (2.37) therefore becomes

$$-\frac{2}{Re}A(e_{ij}E_{ij})\,(e_{ij}E_{ij})^* = -\frac{2}{Re}A|e_{ij}E_{ij}|^2\,. \tag{2.41}$$

For shear-thinning fluids, $n < 1$, the coefficient A is negative and the last term in (2.37) is always positive; it can be seen as an additional production term in the perturbation kinetic energy budget. The opposite is true for shear-thickening fluids.

3. Numerical method and validation

The numerical code used for the stability calculations presented here is a modified version of the code employed by Giannetti & Luchini (2007) and Pralits *et al.* (2010). As a first step, we solve the nonlinear steady Navier–Stokes equations via Newton iterations and compute the base flow. Eigenvalues and eigenmodes of the linearized stability problem are computed via the Arnoldi algorithm with a shift and invert strategy. The solutions of the linear systems involved in the computations of both the base flow and the linear stability are determined by the use of a nonsymmetric multiFrontal sparse LU decomposition (UMFPACK package). The adjoint modes are computed as left eigenvectors of the discrete systems derived from the discretization of the linearized equations. In this way, the sensitivity function can then be computed by the product of the direct and the adjoint fields.

We use a second-order finite-difference code where the Navier–Stokes equations are solved on a staggered Cartesian mesh without considering body-fitted coordinates for the cylinder. The equations are discretized starting from their conservative form. An immersed boundary technique is implemented to impose zero velocity on the cylinder surface: velocities at the grid points near the cylinder surface are forced to those values needed to fulfil the zero velocity condition on the surface by interpolation (see Giannetti & Luchini 2007, for more details). To obtain more accurate results, stretching is implemented to cluster grid cells near the cylinder. Discretization of the viscous terms involving $\dot{\gamma}$ requires special attention: compared to the Newtonian case, a larger stencil is needed to obtain second-order accuracy. Generally, increasing the width of the discretization stencil is not a problem, although the resulting scheme may be more time and memory demanding. However, when an immersed boundary technique is used to impose the boundary conditions on the wall of the cylinder, care must be taken in order to coordinate the interpolation points with those of the discretization so that the solutions inside and outside the cylinder do not affect each other. This is achieved by discretizing the $\dot{\gamma}$ term by one-sided higher-order formulae (second or third order) with stencils having at maximum one point inside the cylinder, exactly as in the interpolation scheme used for the immersed boundary. Tests performed on different geometries confirmed the second-order global accuracy of the adopted scheme.

The geometry and computational domain used are shown in figure 2, where the boundary conditions at the outer boundary are also reported. The cylinder is located symmetrically between the upper and the lower boundaries of the domain and its diameter D is set equal to one. The Cartesian coordinate system has its origin at the centre of the cylinder. In most of the cases, the domain size is chosen to be $L_x = 50$ ($x \in [-15, 35]$) and $L_y = 30$ ($y \in [-15, 15]$). The domain is large enough to satisfy the assumption of unconfined flow. The number of grid points along the x- and y-directions is $n_x = 260$ and $n_y = 180$ respectively. The coordinates (x_i, y_j) of the grid

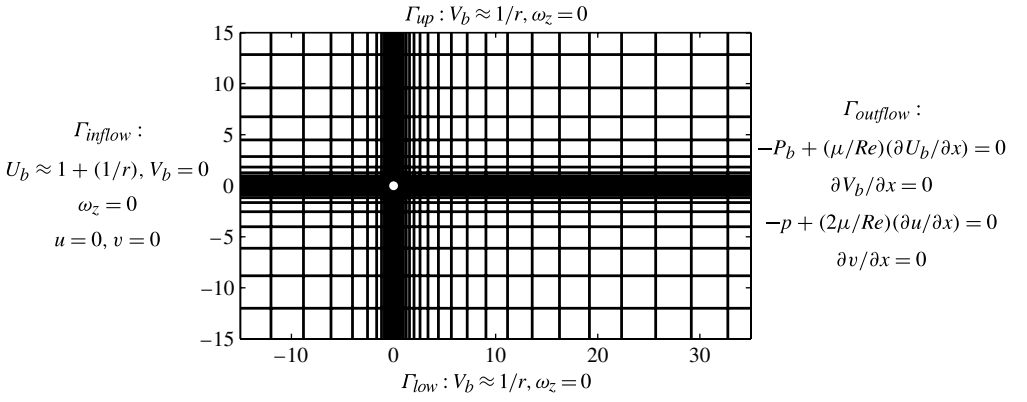

FIGURE 2. Mesh used for the present simulations; only one out of eight lines passing through the pressure nodes are drawn for clarity. The boundary conditions pertaining the outer boundary are also reported for the base flow and perturbation. Zero velocity is imposed at the surface of the cylinder. ω_z, vorticity.

point nodes in the domain are specified as in Giannetti & Luchini (2007),

$$x_i = x_c \left\{ 1 + \frac{\sinh[\tau_x(i/n_x - B_x)]}{\sinh(\tau_x B_x)} \right\} \tag{3.1}$$

and similarly for y_j. In the expression above, B_x is defined as

$$B_x = \frac{1}{2\tau_x} \left[\frac{1 + (\exp(\tau_x) - 1)(x_c/L_x)}{1 + (\exp(-\tau_x) - 1)(x_c/L_x)} \right] \tag{3.2}$$

where x_c (and analogously y_c for the discretization in the cross-stream direction) is the coordinate of the cylinder centre ($x_c = 0, y_c = 0$). τ_x is the stretching parameter and can range from zero for equi-spaced grid points to large values when clustering of the grid cells near the cylinder is desirable. Typically we use 60 stretched grid points in $x \in [-15, -1]$, 60 equi-spaced grid points in $x \in [-1, 1]$ and 140 stretched grid cells in $x \in [1, 35]$ along the streamwise x-direction. In the y-direction, we use 60 stretched grid points in both $y \in [-15, -1]$ and $y \in [1, 15]$ and 60 equi-spaced grid points in $y \in [-1, 1]$.

Boundary conditions are specified as in Giannetti & Luchini (2007) and are listed in figure 2, where U_b, V_b and P_b refer to the base-flow quantities and u, v and p to the velocity perturbation. Zero velocity is imposed at the cylinder surface.

3.1. *Validation*

The code is initially validated against the results by Nouar *et al.* (2007), who ibvestigated the instability of a shear-thinning fluid in channel flow. The results from our code are in perfect agreement with the results of Nouar *et al.* (2007) for the base flow and instability of a parallel flow. As discussed below, stability analysis of the cylinder flow is also validated against nonlinear simulations performed with the spectral-element method.

A parameter study for resolution and domain size is carried out to determine the best grid in terms of accuracy and computational costs. We examine the difference in eigenvalues and critical Reynolds number when increasing resolution from 260×180 to 390×270 grid points in the x–y plane at fixed domain size, and when increasing the

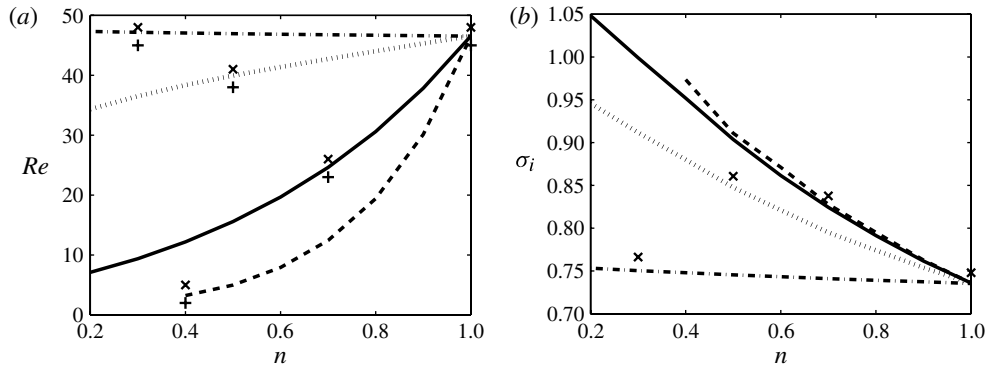

FIGURE 3. (*a*) Neutral curves for *Re*, and (*b*) frequencies σ_i from linear instability analysis versus power index for various λ values: $- \cdot - \cdot -\cdot$, $\lambda = 0.1$; ....., $\lambda = 1$; ——, $\lambda = 10$ and $- - -$, $\lambda = 100$. Symbols indicate results from direct numerical simulations: $\times$, unstable cases; and $+$, stable cases.

domain from $L_x = 50, L_y = 30$ to $L_x = 75, L_y = 45$ with fixed resolution. The difference is below 1 % for all cases and this motivates the choice of the grid whose details have been given above.

3.1.1. *Direct numerical simulation*

To further validate our results we perform direct numerical simulation of the nonlinear equations using the code `Nek5000` (Fischer & Rønquist 1994). This is adapted for the simulation of complex fluids by adding explicit terms that account for the shear-thinning and -thickening. `Nek5000` is based on the spectral-element method (SEM) (Patera 1984). This method has similarities with both finite-element methods (FEM) and spectral methods. The computational domain is sub-divided into a number of elements, where the governing equation is discretized and cast into variational formulation. The solution is approximated by the Galerkin method as an expansion in a finite set of Legendre basis functions, which together with the corresponding Gauss–Lobatto grid enable exact Gaussian quadrature for the evaluation of the element-wise integrals. For the results presented here we used a grid with (56×26) elements and sixth polynomial order and the same computational domain used for linear instability calculation (see figure 2).

4. Results for pseudo-plastic fluids

We investigate shear-thinning and shear-thickening effects on the instability of the cylinder flow. The shear-dependent viscosity is defined by the Carreau model where the shear-thinning effect is more pronounced for low values of power index n and large values of material time constant λ. The power index and the time constant are chosen here in the range $0.4 \leqslant n \leqslant 1.75$ and $0.1 \leqslant \lambda \leqslant 100$. In this section we will consider only shear-thinning fluids ($n < 1$) whereas shear-thickening fluids ($n > 1$) will be considered in the next section. It is relevant to note here that values of $n < 1$ can be shown to match most of experimental observations for polymer solutions (Bird *et al.* 1987).

First we report the critical Reynolds number, the Reynolds number at which the flow first becomes unstable. Stability calculations have been carried out for several values of the spanwise wavenumber β and the first mode to become unstable is found to be a two-dimensional mode, as for a Newtonian fluid, for all cases considered here.

We display the critical values obtained with the Carreau law in figure 3(*a*), where the neutral curves are displayed versus power index n for four different values of the time constant $\lambda = 0.1, 1, 10$ and 100. The shear-thinning effect induces a monotonic decrease of the critical Reynolds number. For the strongest shear-thinning examined, $n = 0.4$ and $\lambda = 100$, the critical Reynolds number decreases from 47 for a Newtonian fluid to $\sim$3. Figure 3(*b*) displays the frequency (imaginary part of the eigenvalue) of the unstable solutions just above the neutral curves. The frequency increases when increasing the shear-thinning from 0.735 for the Newtonian case to 1.04 for $\lambda = 10$ and $n = 0.2$.

The results of the finite-difference stability code have been validated by direct numerical simulation (DNS) using Nek5000. As shown in figure 3(*a*), unstable (time-periodic) and stable solutions are obtained just above and below the neutral curves computed from linear stability for several test cases. In figure 3(*b*) we report the frequency of the periodic limit cycle obtained via DNS. The frequency of the oscillations is also in agreement with the results obtained with the linearized equations and a different spatial discretization. Indeed, close to the neutral point we expect linear stability to predict accurately the frequency of the limit cycle: this is no longer the case further away from the neutral conditions.

4.1. *Base-flow characteristics*

In this section we examine the effect of shear-thinning on the steady base-flow solutions. First, we analyse the shear-thinning effect on the size of the recirculating bubble behind the cylinder. We plot the streamline associated with separation in figure 4(*a*) and, in white, the region delimited by zero velocity for a fixed value of the Reynolds number $Re = 40$, $\lambda = 10$ and different values of n. The recirculation region elongates considerably as shear-thinning becomes stronger: it extends from $\sim$3 diameters behind the cylinder for the Newtonian case ($n = 1$) to $\sim$10 diameters for $n = 0.4$. Figure 4(*b*) displays the streamlines and zero-velocity curve for $\lambda = 10$ along the neutral curve; the recirculation bubble is seen to approach a similar length at critical conditions.

To quantify this effect we report the dimensions of the recirculation bubble versus the Reynolds number for a fixed value of $\lambda = 10$ and different values of n in figure 5. The length of the steady recirculation bubble for Newtonian fluid increases linearly with Reynolds number (Giannetti & Luchini 2007); we show in figure 5(*a*) that this is true also for the values of the power index examined here. In figure 5(*b*), we instead report the width of the recirculation region. The recirculating bubble widens with shear-thinning in all the cases.

The drag coefficient for shear-thinning Carreau cylinder flow with $\lambda = 10$ and several n is displayed in figure 6. In the Newtonian case, the drag coefficient reduces from $\sim$2.7 to 1.5 when the Reynolds number increases from 10 to 40, as already known (see e.g. Kunde & Cohen 1990). Shear-thinning decreases the drag coefficients significantly for all Reynolds numbers between 10 and 40. For a fixed Reynolds number equal to 10 the drag coefficient reduces from 2.7 for the Newtonian case to 1.24 when $n = 0.4$. This observation is in agreement with the results by Patnana *et al.* (2009) at subcritical conditions, who show that for a fixed value of the Reynolds number the drag coefficient of power-law fluids increases with increasing value of power index (n).

Coelho & Pinho (2004) indicate that the reduction in the turbulent shear stresses in the wake of the cylinder is responsible for elongating the recirculation bubble. A similar reduction in drag and elongation of the recirculation bubble is observed here

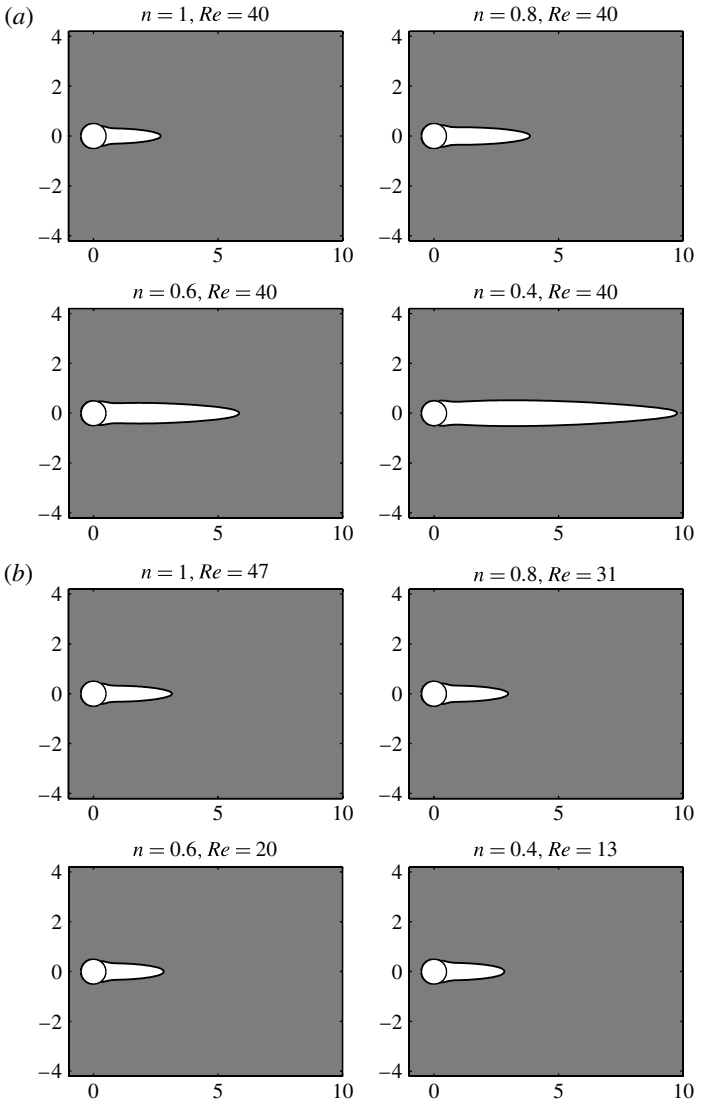

FIGURE 4. Visualization of the recirculation bubble behind the cylinder for different values of the exponent n. (a) $Re = 40$ and $\lambda = 10$, (b) critical values of the Reynolds number for fixed $\lambda = 10$.

for laminar flows. This can be explained by considering the reduction in shear stress, associated with shear-thinning, occurring on the sides of the recirculation region where the largest shear is found. This causes an increase of the pressure behind the cylinder to keep the balance of forces within the recirculation bubble. As shown in figure 4(a), separation does indeed move closer to the top/bottom of the cylinder when decreasing the value of n, which also explains the increase in wake width. The reduction of the shear stress also causes a decrease of the entrainment by the shear layers of fluid from the region behind the cylinder during the transient to the steady state. This elongates the recirculating bubble.

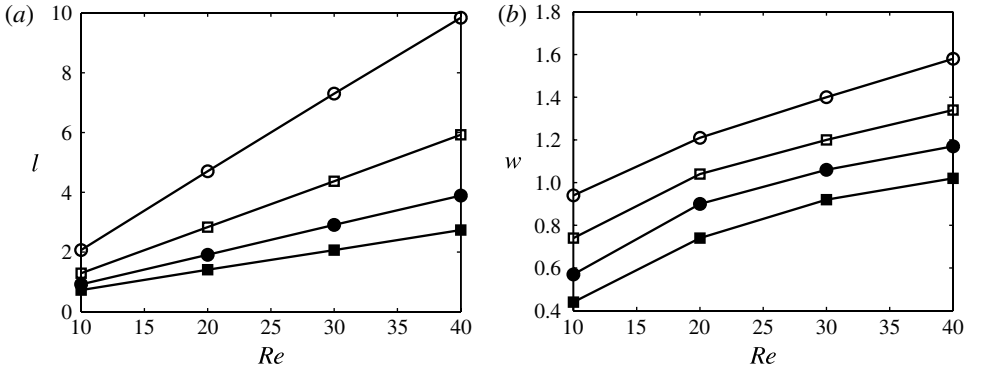

FIGURE 5. (*a*) Bubble length l, and (*b*) bubble width w for fixed $\lambda = 10$: ○, $n = 0.4$; □, $n = 0.6$; ●, $n = 0.8$; ■, $n = 1$.

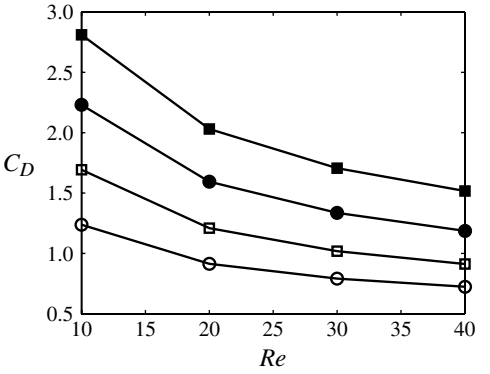

FIGURE 6. Drag coefficient, C_D, versus the Reynolds number, Re, for $\lambda = 10$: ○, $n = 0.4$; □, $n = 0.6$; ●, $n = 0.8$; ■, $n = 1$.

4.2. *Global modes and sensitivity*

The direct and adjoint modes indicate the location of maximum amplitude of the perturbation and the region of highest receptivity respectively. As shown among others by Giannetti & Luchini (2007) for Newtonian fluids, the maximum of the direct modes is reached far downstream of the cylinder surface, while the peak of the adjoint modes is located in the near wake. The characteristics of the direct global modes for shear-thinning fluids are displayed in figure 7 where we show the spatial distribution of the velocity perturbation magnitude at critical Reynolds numbers for $\lambda = 10$ and four different values of n. The largest fluctuations are located far downstream of the cylinder for Newtonian flow, at a distance of $\sim$20 diameters. These peaks move gradually upstream when increasing shear-thinning and are located only 5 diameters downstream of the cylinder for $n = 0.4$: the region where significant fluctuations can be observed also shrinks significantly. As a consequence of this more pronounced localization, the normalized values of the maxima of $\hat{u}$ and $\hat{v}$ increase from 0.008 and 0.013 for $n = 1$–0.022 and 0.02 for $n = 0.4$ (not shown here).

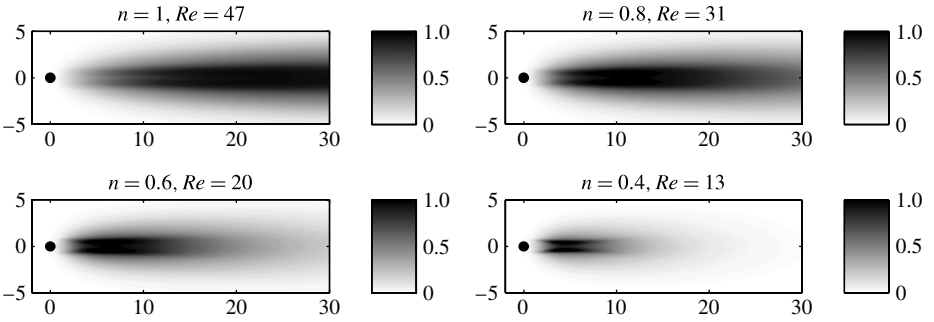

FIGURE 7. Unstable global modes: spatial distribution of the velocity field modulus at the critical Reynolds number for fixed $\lambda = 10$ and four values of n.

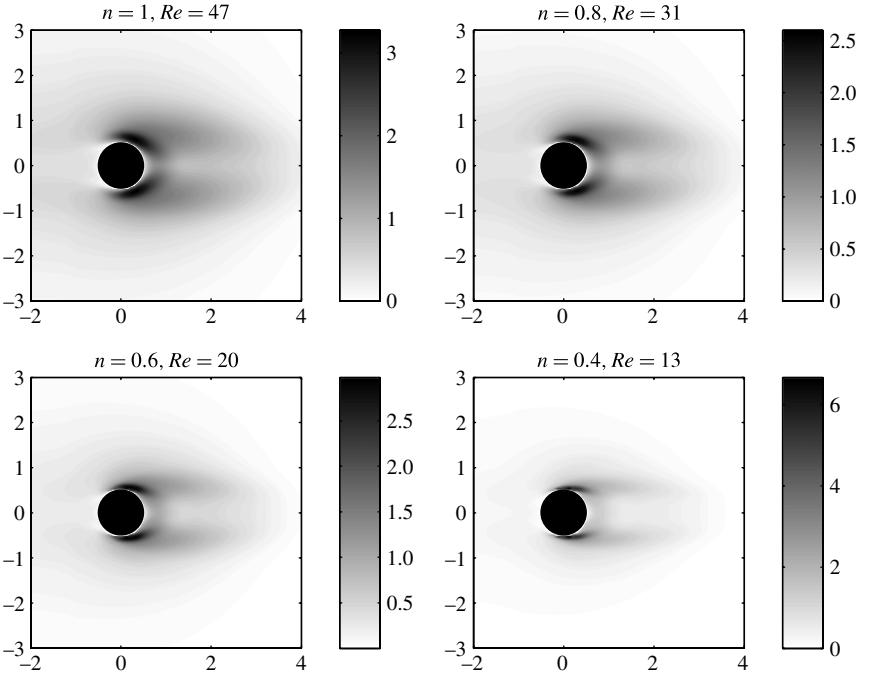

FIGURE 8. Spatial distribution of the magnitude of the adjoint global mode at the critical Reynolds number for a fixed $\lambda = 10$ and four values of n.

The regions most receptive to momentum forcing are visualized in figure 8 by the spatial distribution of the adjoint modes at critical Reynolds number, again for $\lambda = 10$ and for four different values of the shear-thinning exponent n. In all cases, the region of maximum receptivity is localized in the near wake of the cylinder, symmetrically on the upper and lower sides of the cylinder surface. Unlike the direct modes, the adjoint modes decay quickly both upstream and downstream of the cylinder, $x < -2$

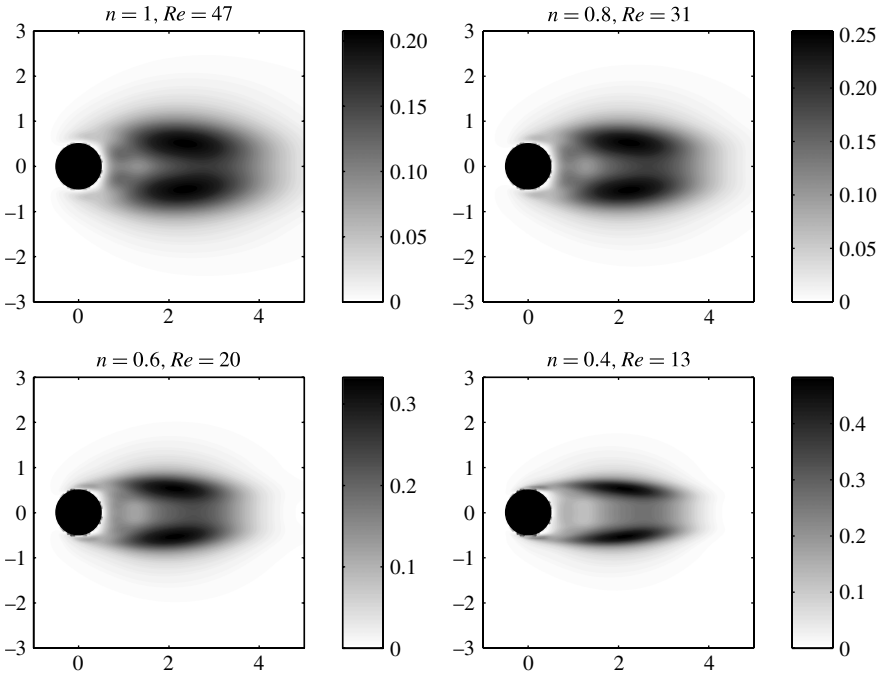

FIGURE 9. Sensitivity map for a fixed $\lambda = 10$ and four values of n along the neutral curve.

and $x > 4$. These characteristics of the adjoint field remain almost constant over the range of values of the rheological parameters examined in this work, although one can notice an increased localization of the peak of the adjoint velocity field when increasing shear-thinning (deceasing n). The differences in the spatial localization of the maxima of the direct and adjoint modes results from the convective non-normality of the Navier–Stokes equations (Chomaz 2005; Sipp *et al.* 2010).

The instability mechanism, however, cannot be deduced from the study of either eigenfunction separately. The onset of instability is generated by a self-exciting mechanism in the region of flow with the role of wavemaker. This wavemaker region can be identified by structural sensitivity analysis of the unstable modes introduced above. The spatial map of the spectral norm of the sensitivity tensor $\boldsymbol{S}$ (see § 2.3, (2.29) and (2.30)) is shown in figure 9 for $\lambda = 10$, again at the critical Reynolds number pertaining to different values of n. Results for different values of the parameter λ would show a similar trend. In all cases, the core of instability consists of two lobes placed symmetrically downstream of the cylinder. Although the spatial separation between the maxima of the direct and adjoint modes decreases with shear-thinning, the main characteristics of the sensitivity field do not change considerably. This finding may be explained by the fact that the size of the recirculation bubble, clearly associated with the instability generation by the sensitivity map in figure 9, is not substantially varying at critical conditions as shown in figure 4(*b*). The most noticeable effect associated with shear-thinning is that the area of maximum sensitivity shrinks when decreasing n while the peak value of the sensitivity function increases

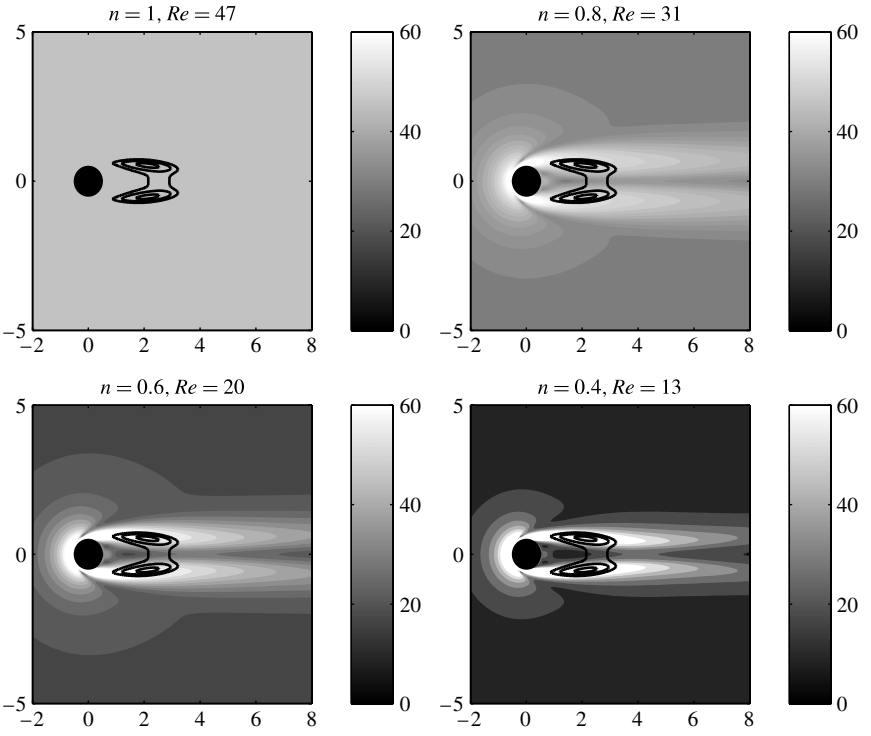

FIGURE 10. Spatial distribution of the local Reynolds number along the neutral curve for $\lambda = 10$ and four values of n. The contour lines represent the regions of largest structural sensitivity.

(note that the sensitivity is obtained at lower nominal Reynolds number for lower values of n).

The viscosity of a shear-thinning fluid varies with the local shear rate ($\mu_{local}(\dot{\gamma}_{local})$). Therefore, a local Reynolds number can be defined as

$$Re_\mu = \frac{\rho U_\infty D}{\mu_{local}}, \tag{4.1}$$

to gain further understanding of the instability mechanism. The spatial distribution of the local Reynolds number Re_μ is depicted in figure 10 for the same parameters considered above. The colour map is fixed for each plot to be in the range between 0 and 60 ($Re = 47$ being the critical value for Newtonian flow). The local Reynolds number appears to be approximately equal to or slightly larger than 47 in the region of largest sensitivity in all cases although the local Reynolds number can significantly decrease just outside the regions of highest shear. The data in the figure therefore confirm that the same physical mechanisms is at work: shear-thinning effects act through significant modification of the base flow at given Reynolds number whereas the instability seems to appear when similar characteristics of the wake are occurring, both in terms of local viscosity and size of the recirculation bubble.

Index n	1.75	1.5	1.25	1	0.8	0.6	0.4
$\lambda = 1$	47.17	47.16	46.85	47	48	48.6	50.32
$\lambda = 10$	48.72	47.84	47.39	47	46.98	46.96	48.63
$\lambda = 100$	48.7	47.62	47.15	47	47.76	47.5	49.375

TABLE 1. Stability Reynolds number $\overline{Re}$ along the neutral curves (note that shear-thickening results are also reported here).

To corroborate this observation, we define an average viscosity using the square of the sensitivity function as weight

$$\overline{\mu} = \frac{\int_D \mu(x, y) S(x, y)^2 \, \mathrm{d}A}{\int_D S(x, y)^2 \, \mathrm{d}A}, \tag{4.2}$$

where D is the computational domain, S is the sensitivity defined above. An instability Reynolds number can thus be defined as

$$\overline{Re} = \frac{\rho U_\infty D}{\overline{\mu}}. \tag{4.3}$$

Table 1 shows the value of this stability Reynolds number along the neutral curves: a value close to 47 is found for all cases (this applies also to shear-thickening fluids discussed in the next section).

Sensitivity analysis of base-flow modification provides information about the effect of base flow on the instabilities and the role of passive control devices. The spatial distribution of the structural sensitivity due to base-flow modifications is presented in figure 11, for $\lambda = 10$ at four critical Reynolds numbers (see § 2.3.1). For all the cases, the sensitivity to base-flow modifications is considerably stronger than that to structural perturbations, as shown by Giannetti & Luchini (2007) for a Newtonian fluid. For example, for a value $n = 0.4$ of the power index and $\lambda = 10$, the maximum value of the sensitivity to base-flow modification is $\sim$4 while it is $\sim$0.5 for time-dependent structural perturbations. The area of maximum sensitivity is localized close to the cylinder surface, on the upper and lower sides. As for the wavemaker in figure 9, shear-thinning effects do not change the main features of the sensitivity map: the area of maximum sensitivity becomes thinner while the magnitude increases when decreasing n.

4.3. *Energy analysis*

The instability mechanism is now examined by considering the perturbation kinetic energy budget. Figure 12 shows the contribution from the different terms in the energy budget (2.37) integrated over the computational domain. The data pertain to fixed Reynolds number $Re = 20$ and $\lambda = 10$. The magnitude of the production and viscous dissipation terms decreases with the power index n, whereas the additional positive contribution related to shear-thinning effects becomes significant only for $n \lesssim 0.5$. The sum of the two production terms and of viscous dissipation, normalized with the total kinetic energy of the mode, yields the temporal growth rate (solid line in the figure); it crosses the value of zero for $n \approx 0.6$, the value of the critical Reynolds number presented above.

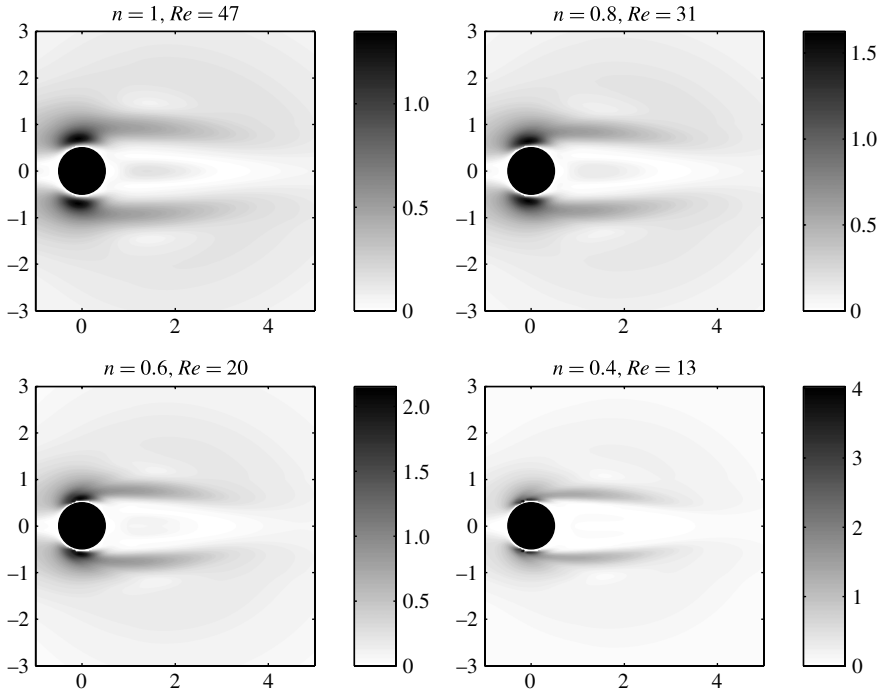

FIGURE 11. Sensitivity map due to base-flow modifications for a fixed $\lambda = 10$ along the neutral curve.

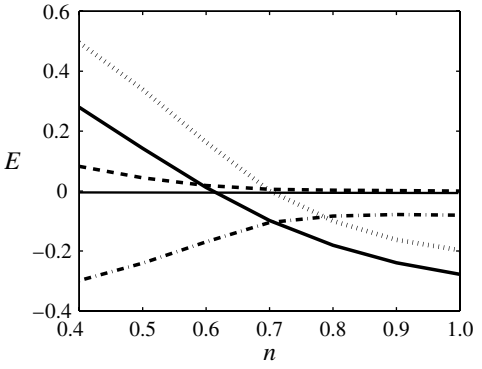

FIGURE 12. Integral of production and dissipation of perturbation kinetic energy E over the domain for a fixed $\lambda = 10$ and $Re = 20$: $- \cdot - \cdot -\cdot$, dissipation; ....., production; $- - -$, shear-thinning production; and —, sum.

The spatial distribution of the total kinetic energy production of the perturbation is reported in figure 13. Here, one can distinguish regions of positive and negative production. We notice that the positive production becomes more and more localized with increasing shear-thinning and the magnitude of the peak production increases. The region of large sensitivity is also reported in the figure and related to that of largest energy production: for Newtonian flow and the largest values of n,

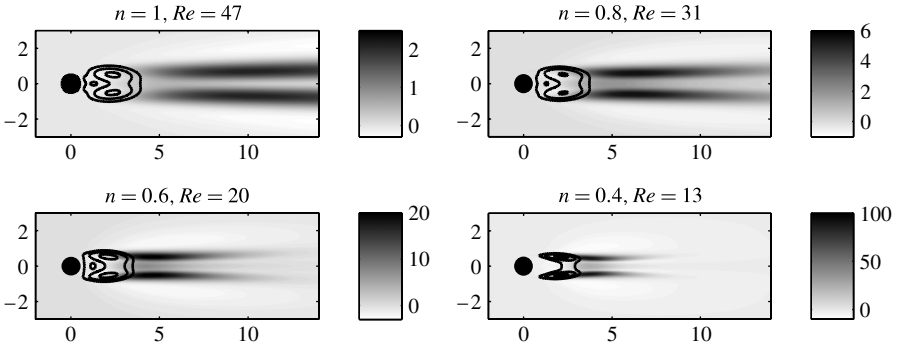

FIGURE 13. Spatial distribution of the sum of the total production and dissipation of perturbation kinetic energy, normalized by the energy of perturbation, plotted together with the contour level delimiting the area of maximum structural sensitivity at critical Reynolds number for $\lambda = 10$.

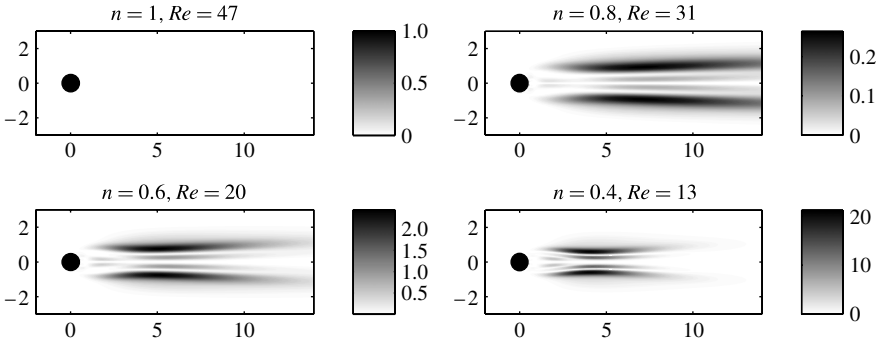

FIGURE 14. Spatial distribution of the additional production of perturbation kinetic energy, $-(2/Re)A|e_{ij}E_{ij}|^2$, for a fixed $\lambda = 10$ along the neutral curve, normalized by the energy of perturbation.

the wavemaker is clearly located upstream of the region of largest production of fluctuation energy. Only for the lowest value of n examined do the two regions partially overlap. As discussed e.g. in Pralits *et al.* (2010), structural sensitivity and kinetic energy budget provide different information about the instability process. The former identifies the region where the unstable perturbation is created (the pocket of absolute instability in a weakly non-parallel context) while the latter identifies where the largest amplification is attained (a region of strong convective instability in a weakly non-parallel flow).

As introduced in § 2.3.2, an additional production term, strictly positive, appears in the case of shear-thinning fluids, $-(2/Re)A|e_{ij}E_{ij}|^2$. Its spatial distribution is displayed in figure 14 for the same fluid considered in figure 13. This extra production term is zero everywhere in the domain for $n = 1$ and gradually increases with the magnitude of the shear-thinning effects. The location and extent of the density of the additional production are very similar to those of the total production displayed in figure 13. The total production of kinetic energy is largest downstream of the region of largest structural sensitivity. The perturbations originate inside the wavemaker and propagate

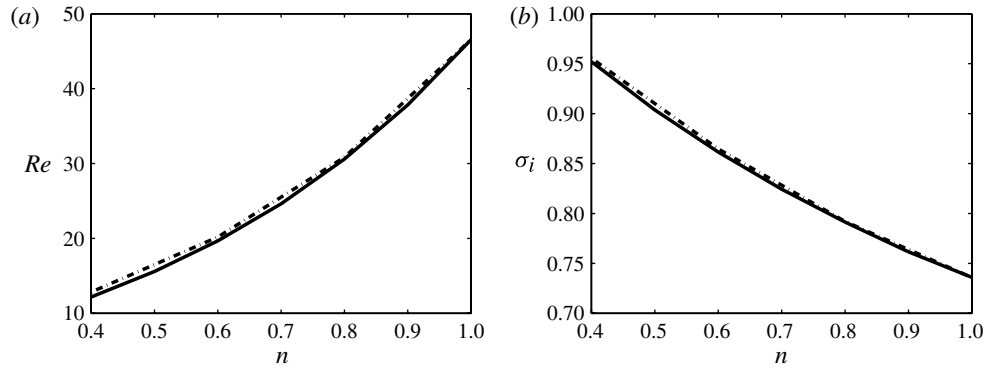

FIGURE 15. Effect of the viscosity disturbance in the perturbation equations. (*a*) Neutral stability curve and (*b*) frequency of the least-stable mode at critical conditions for $\lambda = 10$: —, including viscosity disturbance; $- \cdot - \cdot -\cdot$, excluding viscosity disturbance.

as waves downstream. They are most amplified further downstream where the largest production is found.

4.4. *Viscosity fluctuation*

Nouar *et al.* (2007) note that to assess whether there is stabilization and by how much in the presence of shear-dependent viscosity, it is important to account for a viscosity fluctuation in the perturbation equations; failure to do so can yield qualitatively and quantitatively incorrect conclusions. This is demonstrated by these authors, at least for the case of plane channel flow where the critical Reynolds numbers are about a factor 2 larger when the viscosity perturbation is not taken into account. In this section we therefore investigate in further detail the effect of viscosity fluctuation (μ') on the instability mechanism for the flow past a circular cylinder. The results of stability calculations performed excluding a viscosity disturbance in the perturbation equations are reported in figure 15, where both the critical Reynolds number and the frequency of the least-stable mode are displayed. The flow is slightly stabilized only at the smallest small values of the power exponent n when excluding μ' from the equations. We can therefore conclude that the viscosity fluctuation has no effect on the first bifurcation for the flow past a cylinder of a shear-thinning fluid.

5. Dilatant fluids

In this section we examine the instability of dilatant or shear-thickening fluids flowing past a circular cylinder. In contrast with the shear-thinning fluid, the viscosity of the shear-thickening fluids increases with the shear rate of the flow. This behaviour is described by the Carreau model when the power index $n > 1$.

The critical Reynolds number versus the exponent n for a shear-thickening fluid is shown in figure 16(*a*), where we display data for four different values of the time constant $\lambda = 0.1, 1, 10$ and 100. The shear-thickening effect stabilizes the cylinder flow dramatically when considering the Reynolds number based on the zero-shear-rate viscosity. For $n = 1.4$ and $\lambda = 10$, the critical Reynolds number increases from 47 for a Newtonian fluid to $\sim$102. The symbols in the figure represent results obtained by DNS of the full nonlinear Navier–Stokes equations and validate the linear stability analysis. The results are consistent with those obtained for shear-thinning fluids; in

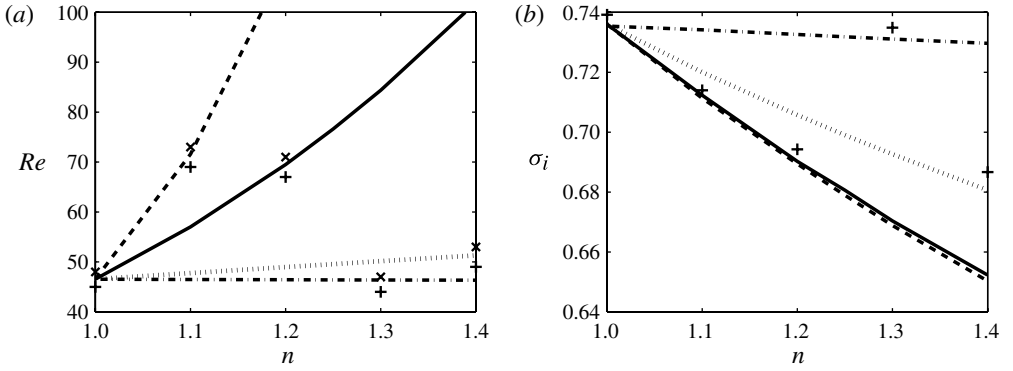

FIGURE 16. (*a*) Neutral curves and (*b*) frequency of the least-stable mode for shear-thickening cylinder flow: $- \cdot - \cdot - \cdot$, $\lambda = 0.1$; ....., $\lambda = 1$; —, $\lambda = 10$ and $- - -$, $\lambda = 100$. Symbols indicate results from direct numerical simulations: +, unstable cases and ×, stable cases.

this case the increase of the local viscosity prevents the formation of a sufficiently long recirculation bubble and thus delays the onset of the unsteady flow. Figure 16(*b*) displays the frequencies of the solutions just above the neutral curve. The frequency of the unstable modes decreases from 0.735 for the Newtonian case to 0.65 for $\lambda = 10$ and $n = 1.4$.

The structural sensitivity and the local Reynolds number Re_μ are reported in figure 17 for different values of the exponent n. As for the case of shear-thinning fluids, the region of largest sensitivity, the wavemaker, does not vary with the magnitude of the non-Newtonian effects. One can just note an increase of the area of maximum sensitivity for increasing n. The local viscosity can decrease to yield a local value $Re_\mu \approx 50$ at the core of the instability although it may be lower (higher Re_μ) in the region further downstream. Indeed, as reported in table 1, the stability Reynolds number $\overline{Re}$ obtained by averaging the local Re_μ with the structural sensitivity is $\sim$47 also for shear-thickening fluids. The sensitivity of shear-thickening fluids to base-flow modifications presents the same characteristics as that of shear-thinning fluids. Further, as noted here for the wavemaker, the area of maximum sensitivity increases while the magnitude of the sensitivity decreases on increasing the power index n. In summary, the physical mechanisms associated with the reduction of the critical Reynolds number discussed for shear-thinning fluids can be applied, in the opposite direction, to the behaviour of shear-thickening fluids.

6. Discussion and conclusions

We have investigated the onset of the first instability for the flow past a circular cylinder of shear-thinning and shear-thickening fluids. The shear-dependent viscosity is modelled by the Carreau law where the rheological parameters, i.e. the power index and the material time constant, are chosen in the range $0.4 \leqslant n \leqslant 1.75$ and $0.1 \leqslant \lambda \leqslant 100$. Structural sensitivity analysis based on the idea of a wavemaker is used to identify the core of the instability. Sensitivity analysis to base-flow modifications is employed to investigate the effect of a local steady forcing on the instability. Perturbation kinetic energy budget is also considered to examine the physical mechanisms responsible for the production of the instability. This work

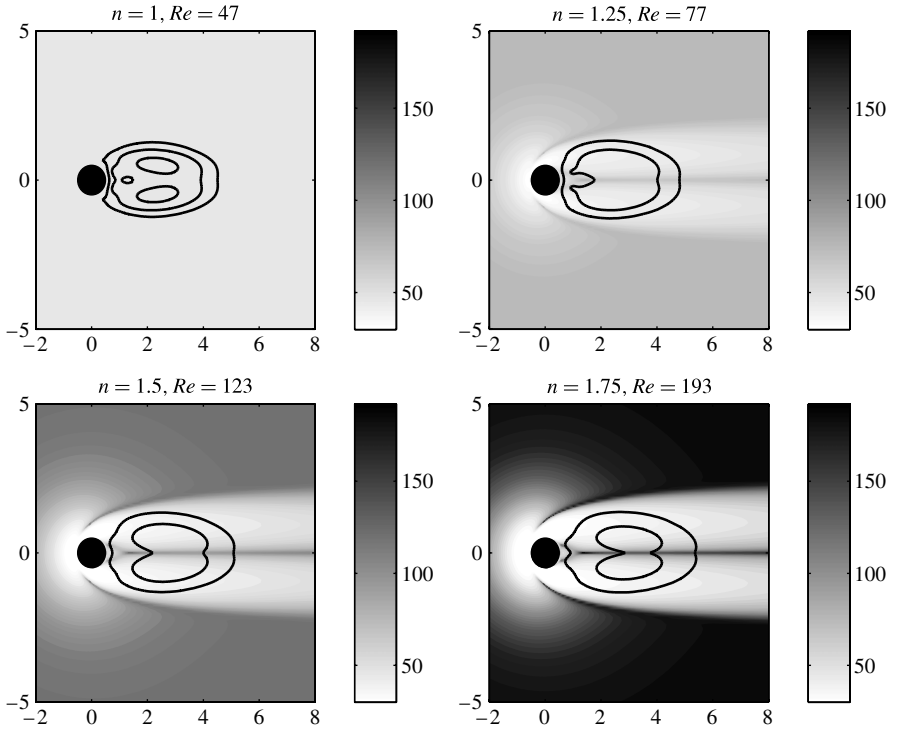

FIGURE 17. Spatial distribution of the local Reynolds number along the neutral curve for $\lambda = 10$ and values of n listed on each plot. The contour lines represent the regions of largest structural sensitivity.

presents the first global linear stability analysis of non-Newtonian fluids for the configuration examined. The main conclusions can be summarized as follow.

It is observed that the first bifurcation occurs in all cases considered for two-dimensional modes, as for the Newtonian case. Floquet analysis of the instability of the limit cycle at higher Reynolds numbers is therefore a relevant extension of the present study. The shear-thinning effect destabilizes the cylinder flow dramatically when defining the Reynolds number with the zero-shear-rate viscosity. For the strongest shear-thinning effect, $n = 0.4$ and $\lambda = 100$, the critical Reynolds number decrease from 47 for a Newtonian fluid to $\sim$3. The frequency of the unsteady solutions computed via DNS just above the neutral curves increases with shear-thinning from 0.735 for the Newtonian case to 1.04. In the case of shear-thickening fluids, the critical Reynolds number increases with the time constant λ and the exponent n. For $n = 1.75$ and $\lambda = 10$, the critical Reynolds number increases from 47 for Newtonian fluids to $\sim$193. The corresponding frequencies of the solutions just above the neutral curve decreases from 0.735 to 0.65. The numerical simulation of the full nonlinear equations also provides a validation for the results presented.

The direct and adjoint modes indicate the location of maximum amplitude of the perturbation and the region of highest receptivity in the flow field. The maxima of the direct global modes are located far downstream of the cylinder for Newtonian flow and move gradually upstream with shear-thinning when considering the flow just above critical conditions. In all the cases, the regions of maximum receptivity

are localized in the near wake, close to the upper and lower sides of the cylinder surface. The wavemaker, the core of the instability, is found to be in the two lobes placed symmetrically downstream of the cylinder, similarly to what is found in the Newtonian case (Giannetti & Luchini 2007; Marquet *et al.* 2008). The area of maximum sensitivity becomes more and more localized when increasing shear-thinning effects, while it becomes more diffuse for shear-thickening fluids. The region of maximum sensitivity to base-flow modifications is found close to the cylinder surface in the upper and lower sides for all the cases examined.

The total production of perturbation kinetic energy is largest downstream of the region of the wavemaker. The perturbations originate from the region of the wavemaker and are most amplified further downstream where the largest production is observed, possibly due to strong shear rate. We further examine the effect of the viscosity fluctuation (μ') on the instability of the flow past a cylinder, and analysis of the perturbation kinetic energy budget reveals that an additional production term is originated in the presence of shear-dependent viscosity. This term is strictly positive for shear-thinning fluids and negative for shear-thickening fluids. We demonstrate that μ' does not affect the neutral curves nor the core of instability. However it is responsible for increased amplification of the disturbance kinetic energy downstream of the region of the wavemaker in the case of shear-thinning fluids, while the opposite applies to dilatant fluids.

As the instability mechanism is not changed significantly by shear-thinning and shear-thickening, we explain the difference in critical Reynolds number by the effect that the non-Newtonian character of the fluid has on the steady base flow. We show that the drag coefficient decreases significantly with shear-thinning for Reynolds numbers between 10 and 40. The recirculating bubble behind the body elongates considerably with the shear-thinning effect, while it shortens for shear-thickening fluids. As an example, at $Re = 40$, the bubble extends from $\sim$3 diameters for the Newtonian case to 10 diameters for $n = 0.4$ and $\lambda = 10$. The shear-thinning effects also intensifies the magnitude of vorticity in the region close to the cylinder surface. These effects can be explained by considering the reduction in shear stress, associated with shear-thinning, occurring in the regions of largest shear on the sides of the recirculation region.

Most importantly, we show that at critical conditions the recirculation region approaches the same size for all cases considered here. Thus, there appears to be a critical configuration of the wake for the onset of the instability, which is then mainly of inviscid type. These critical conditions are determined by the local viscosity creating the separation region. We displayed the spatial distribution of a local Reynolds number based on the local value of the viscosity. Along the neutral curves, we did indeed find that the same region around the cylinder represents Reynolds number equal to or around 47 for both pseudo-plastic and dilatant fluids. This region where the local $Re_\mu \approx 50$ overlaps significantly with the area of largest structural sensitivity.

Nouar *et al.* (2007) discuss the importance of the choice of the viscosity used to define the Reynolds number; the conclusions when comparing results for fluids with different rheological properties, including Newtonian fluids, can indeed depend on the choice of the viscosity scale. They argue that the tangent viscosity evaluated at the wall is a more relevant choice than the average effective viscosity for the case of plane channel flow. The extension to an open configuration like that considered here is not straightforward: an effective viscosity averaged over all the domain is certainly not useful as the core of the instability is localized in the near wake. In the

same spirit, the shear stress at the wall may not be that relevant for separating flows where pressure gradient effects are more relevant. Therefore here we decided to define a stability Reynolds number obtained as a weighted average of the local Reynolds number over the whole domain where the weight function is the norm of the structural sensitivity. In this way we obtain a value of the critical Reynolds number of $\sim$47 for all cases considered.

This study represents a first theoretical analysis of the instability mechanisms in the wake past a solid bluff body for inelastic non-Newtonian fluids. The work can therefore be extended to consider a confined object (Camarri & Giannetti 2007, 2010), as well as an array of objects (Nejat *et al.* 2011).

Acknowledgements

F.G. acknowledges financial support from the C. M. Lerici Foundation during his visit to Stockholm. Computer time provided by SNIC (Swedish National Infrastructure Centre) is gratefully acknowledged. We would like to thank P. Luchini for the CPL compiler.

REFERENCES

ALIZARD, F., ROBINET, J.-C. & RIST, U. 2010 Sensitivity analysis of a streamwise corner flow. *Phys. Fluids* **22** (1), 014103.

BARKLEY, D. & HENDERSON, R. D. 1996 Three-dimensional Floquet stability analysis of the wake of a circular cylinder. *J. Fluid Mech.* **322**, 215–241.

BIRD, R. B., CURTISS, C. F., ARMSTRONG, R. C. & HASSAGER, O. 1987 *Dynamics of Polymeric Liquids*, 2nd edn. Wiley-Interscience.

BOTTARO, A., CORBETT, P. & LUCHINI, P. 2003 The effect of base flow variation on flow stability. *J. Fluid Mech.* **476**, 293–302.

BRANDT, L., SIPP, D., PRALITS, J. O. & MARQUET, O. 2011 Effect of base-flow variation on non-modal stability. *J. Fluid Mech.* **687**, 503–528.

CAMARRI, S. & GIANNETTI, F. 2007 On the inversion of the von Karman street in the wake of a confined square cylinder. *J. Fluid Mech.* **574**, 169–178.

CAMARRI, S. & GIANNETTI, F. 2010 Effect of confinement on three-dimensional stability in the wake of a circular cylinder. *J. Fluid Mech.* **642**, 477–487.

CATON, F. 2006 Linear stability of circular Couette flow of inelastic viscoplastic fluids. *J. Non-Newtonian Fluid Mech.* **134**, 148–154.

CHOMAZ, J.-M. 2005 Global instabilities in spatially developing flows: non-normality and nonlinearity. *Annu. Rev. Fluid Mech.* **37**, 357–392.

COELHO, P. M. & PINHO, F. T. 2003*a* Vortex shedding in cylinder flow of shear-thinning fluids. I identification and demarcation of flow regimes. *J. Non-Newtonian Fluid Mech.* **110**, 143–176.

COELHO, P. M. & PINHO, F. T. 2003*b* Vortex shedding in cylinder flow of shear-thinning fluids. II flow characteristics. *J. Non-Newtonian Fluid Mech.* **110**, 177–193.

COELHO, P. M. & PINHO, F. T. 2004 Vortex shedding in cylinder flow of shear-thinning fluids. III pressure measurements. *J. Non-Newtonian Fluid Mech.* **121**, 55–68.

FISCHER, P. F. & RØNQUIST, E. M. 1994 Spectral element methods for large scale parallel Navier–Stokes calculations. *Comput. Meth. Appl. Mech. Engng* **116**, 69–76.

GIANNETTI, F. & LUCHINI, P. 2007 Structural sensitivity of the first instability of the cylinder wake. *J. Fluid Mech.* **581**, 167–197.

KUNDE, P. K. & COHEN, I. M. 1990 *Fluid Mechanics*. Elsevier.

MARQUET, O., LOMBARDI, M., CHOMAZ, J.-M., SIPP, D. & JACQUIN, L. 2009 Direct and adjoint global modes of a recirculation bubble: lift-up and convective non-normalities. *J. Fluid Mech.* **622**, 1–21.

MARQUET, O., SIPP, D. & JACQUIN, L. 2008 Sensitivity analysis and passive control of cylinder flow. *J. Fluid Mech.* **615**, 221–252.

MELIGA, P., SIPP, D. & CHOMAZ, J.-M. 2010*a* Effect of compressibility on the global stability of axisymmetric wake flows. *J. Fluid Mech.* **660**, 499–526.

MELIGA, P., SIPP, D. & CHOMAZ, J.-M. 2010*b* Open-loop control of compressible afterbody flows using adjoint methods. *Phys. Fluids* **22** (5), 054109.

MILLETA, S., ROUSSET, F. & HADID, V. B. H. B. 2009 Stability analysis of stratified coating flow of shear-thinning fluids. *Eur. Phys. J. Special Topics* **166**, 143–146.

MOSSAZ, S., JAY, P. & MAGNIN, A. 2010 Criteria for the appearance of recirculating and non-stationary regimes behind a cylinder in a viscoplastic fluid. *J. Non-Newtonian Fluid Mech.* **165**, 1525–1535.

NEJAT, A., ABDOLLAHI, V. & VAHIDKHAH, K. 2011 Lattice Boltzmann simulation of non-Newtonian flows past confined cylinders. *J. Non-Newtonian Fluid Mech.* **166**, 689–697.

NOUAR, C., BOTTARO, A. & BRANCHER, J. P. 2007 Delaying transition to turbulence in channel flow: revisiting the stability of shear-thinning fluids. *J. Fluid Mech.* **592**, 177–194.

NOUAR, C. & FRIGAARD, I. 2009 Stability of plane Couette-Poiseuille flow of shear-thinning fluid. *Phys. Fluids* **21**, 064104.

PANDA, S. K. & CHHABRA, R. 2010 Laminar flow of power-law fluids past a rotating cylinder. *J. Non-Newtonian Fluid* **165**, 1442–1461.

PATERA, A. T. 1984 A spectral element method for fluid dynamics: laminar flow in a channel expansion. *J. Comput. Phys.* **54**, 468–488.

PATNANA, V. K., BHARTI, R. P. & CHHABRA, R. P. 2009 Two-dimensional unsteady flow of power-law fluids over a cylinder. *Chem. Engng Sci.* **64**, 2978–2999.

PIPE, C. J. & MONKEWITZ, P. A. 2006 Vortex shedding in flows of dilute polymer solutions. *J. Non-Newtonian Fluid Mech.* **139**, 54–67.

PRALITS, J. O., BRANDT, L. & GIANNETTI, F. 2010 Instability and sensitivity of the flow around a rotating circular cylinder. *J. Fluid Mech.* **650**, 513–536.

PROVANSAL, M., MATHIS, C. & BOYER, L. 1987 Bénard-von Kármán instability: transient and forced regimes. *J. Fluid Mech.* **182**, 1–22.

RICHTER, D., IACCARINO, G. & SHAQFEH, E. S. G. 2010 Simulations of three-dimensional viscoelastic flows past a circular cylinder at moderate Reynolds numbers. *J. Fluid. Mech.* **651**, 415–442.

RICHTER, D., SHAQFEH, E. S. G. & IACCARINO, G. 2011 Floquet stability analysis of viscoelastic flow over a cylinder. *J. Non-Newtonian Fluid Mech.* **166**, 554–565.

SARPKAYA, T., RAINEY, P. G. & KELL, R. E. 1973 Flow of dilute polymer solution about circular cylinder. *J. Fluid Mech.* **57**, 177–208.

SIPP, D., MARQUET, O., MELIGA, P. & BARBAGALLO, A. 2010 Dynamics and control of global instabilities in open flows: a linearized approach. *Appl. Mech. Rev.* **63**, 030801.

SIVAKUMAR, P., BHARTI, R. P. & CHHABRA, R. 2006 Effect of power-law index on critical parameters for power-law flow across an unconfined circular cylinder. *Chem. Engng Sci.* **61**, 6035–6046.